

Adaptive Mesh Refinement and Error Estimate for 3-D Seismic Analysis of Liquefiable Soil Considering Large Deformation

Xiaowei TANG and Tadanobu SATO

Disaster Prevention Research Institute, Kyoto University, Uji Kyoto 611-0011, Japan

(Received for 28. Sep., 2004 and in revised from 27 Dec., 2004)

ABSTRACT

The focus of this paper is on 3-D adaptive analysis method of liquefiable soil improvement of the approximate quality of nonlinear numerical simulation of the liquefaction process with large deformation. This adaptive technique was applied to the 3-D non-linear FE analysis of liquefiable soil considering large deformation, including the liquefaction phenomenon. The cyclic elasto-plastic model and updated Lagrangian formulation were adopted in the three-dimensional FE analysis. The fission procedure belonging to the h -refinement indicated by the error estimator, a posteriori error estimate procedure depending on L_2 -norm of strain and superconvergent patch recovery method, was used. The convergence of this error estimate scheme and the effectiveness of h -adaptive mesh refinement were shown by simple examples. The adaptive FE method was applied to the three-dimensional practical seismic analysis of an embankment constructed on liquefiable soil, and its efficacy demonstrated in detail. Application of the adaptive technique to the nonlinear analysis of saturated soil, including the liquefaction process, is a valuable step in the three-dimensional seismic analysis of liquefaction.

1. INTRODUCTION

Such soil structures as river dikes, high way embankments and earth dams frequently have been damaged during major earthquakes, often due to liquefaction of embankments and foundation soils. In most cases, unacceptable, large, permanent deformation has occurred due to liquefaction of the supporting, loose, cohesionless foundation soil. The seismic design of soil structures in these liquefiable soils poses very difficult problems for analysis and design. The possibility of liquefaction necessitates further investigation not only experimentally but by numerical analysis.

In computational analysis, saturated soil is described as a type of porous media. Biot's two-phase mixture theory leads to the application of an effective nonlinear finite element method through derivation of the governing equations expressed by u-p formulation; for example, a finite element and finite difference (FE-FD) coupled scheme (Akai and Tamura, 1978). That scheme used to analyze liquefaction with infinitesimal strain condition, reduces the total degree of freedom of the coupled equations. It avoids shear locking under the undrained condition and involves less computational effort than the generalized finite element method. An appropriate constitutive model also is important in the nonlinear analysis of saturated soil. Many effective constitutive models have been developed in recent decades. The cyclic elasto-plastic model (Oka, 1992) is one of most effective. It was proposed as a numerical method to simulate the liquefaction of saturated soils and is based on the non-linear kinematic hardening rule. Because deformation caused by liquefaction usually is very large, the finite deformation theory was introduced to the finite element method. Further development of the FE-FD coupled scheme was achieved in two- and three-dimensional analysis by use of the updated Lagrangian for-

mulation (Sato and Di, 2001; Tang and Sato, 2002). The cyclic elasto-plastic model was adopted as the constitutive model of liquefiable soil in FE-FD coupled scheme used in the study reported here. The material nonlinearity of saturated sand is simulated effectively by the constitutive model. The updated Lagrangian formulation, which belongs to the finite deformation theory, also was applied to the three-dimensional FE-FD coupled scheme to deal with the geometrical nonlinearity of liquefiable soil caused by large deformation.

As a numerical approximation method, errors are inevitable in analytical results obtained by the finite element method. Solutions do not always produce the desired accuracy, sometimes presenting serious analysis problems, especially when considering large deformation. Such error is caused by discretization in the FEM process. In practical problems of liquefied soil flow caused by earthquakes, soil deformation is not uniform and where large deformation is developed can not be predicted. With elements that have large deformation, large numerical error develops. Evidently, uniformly reducing element size during discretization minimizes error, but the number of nodes and elements are increased at the same time, producing a heavy calculation burden. In fact, a region with small deformation does not require a finer mesh. It is better to use a fine mesh in a region with large error and a normal or coarse mesh in a low-error region. A method called the adaptive technique or adaptive mesh refinement has been developed and utilized to reduce discretization error. It has been used successfully in many fields, including solid and fluid mechanics, to linear and nonlinear problems and to solve static and transient behavior of two-dimensional continua. Extension to three-dimensional, dynamic applications, however, is in its infancy. It is still a major challenge to apply adaptive mesh refinement to the seismic analy-

sis of liquefaction.

A posteriori error estimate based on the L_2 norm of strain error was adopted in the adaptive analysis used in our study. It effectively estimates the element error after each calculation step in the nonlinear FE analyses of soil. The superconvergent patch recovery technique (Zienkiewicz and Zhu, 1992) was used in the error estimates. The convergence of this error estimate method was tested in two load cases for a simple example with different quality meshes. Convergence ratios obtained by our method agree with the predicted values. The fission procedure of h -refinement, indicated by the error estimates of the elements in adaptive analysis, was used. The approximation was refined successively so as to satisfy the predetermined standard of accuracy. The efficacy of this method was confirmed for another simple example of consolidation of saturated soil.

Lastly, a practical example of seismic analysis of an embankment, based on the finite deformation theory, was determined with the adaptive FE method. Adaptive analysis results for mesh deformation, error distribution, average error history, and displacement responses were obtained and compared with results calculated without the adaptive procedure. The efficacy of three-dimensional adaptive analysis also was demonstrated by means of practical example.

2. GOVERNING EQUATIONS USING THE UPDATED LAGRANGIAN FORMULATION

2.1 Constitutive equation

In this research, the effective cyclic elasto-plastic constitutive model was used to describe the non-linear behavior of saturated soils. The deformation tensor rate is suitable for application to a constitutive law because it vanishes when the body has rigid-body motion. The stress rate used for a constitutive law therefore must be invariable with respect to rigid-body rotation. The material derivative $d\sigma_{ij}/dt$ does not, in general, satisfy invariance due to rigid-body rotation. To extend this model to a large deformation problem it is necessary to use an invariant stress rate with respect to rigid-body rotation for the constitutive relations. The Jaumann effective stress rate, an objective measure of the stress rate, was;

$$\dot{\sigma}'_{ij} = \dot{\sigma}'_{ij} - \sigma'_{ik}\omega_{jk} - \sigma'_{kj}\omega_{ik} \quad (1)$$

where σ'_{ij} is the effective Cauchy stress, $\dot{\sigma}'_{ij}$ the effective Cauchy stress rate, and ω_{ij} the antisymmetric spin tensor.

Generally, large deformation cannot be expressed linearly in terms of displacements, because the elastic and plastic parts of the deformation rate are not summable. If each time step in the updated Lagrangian analysis is small enough, the total Lagrangian strain rate \dot{E}_{ij} can be decomposed into the elastic component, \dot{E}_{ij}^e , and the plastic component, \dot{E}_{ij}^p .

The linear relationship between the objective stress and deformation rates (i.e., the effective stress-strain law) is

$$\dot{\sigma}'_{ij} = \dot{\sigma}'_{ij} - \dot{p}\delta_{ij} = D_{ijkl}^{ep}\dot{\epsilon}_{kl} - \dot{p}\delta_{ij} \quad (2)$$

where \dot{p} is the rate of pore pressure, and D_{ijkl}^{ep} the elasto-plastic tensor of the cyclic elasto-plastic constitutive model.

2.2 Equilibrium equation

According to Biot's two-phase mixture theory, the local equilibrium equation of motion for the total saturated porous media is

$$\frac{\partial \sigma_{ji}}{\partial x_j} + \rho b_i - (1-n)\rho^s \dot{v}_i^s - n\rho^f \dot{v}_i^f = 0 \quad (3)$$

where v_i^s is the velocity of the soil skeleton, v_i^f the velocity of the fluid phase, n the porosity, ρ the mixture density, ρ^s the solid phase density and ρ^f the liquid phase density.

The average seepage velocity \dot{w}_i is

$$\dot{w}_i = n(v_i^f - v_i^s) \quad (4)$$

Substituting Eq.(4), Eq.(3) is rewritten

$$\frac{\partial \sigma_{ji}}{\partial x_j} + \rho b_i - \rho \ddot{u}_i - \rho^f \left(\frac{\partial \dot{w}_i}{\partial t} + \dot{w}_k \dot{w}_{i,k} \right) = 0 \quad (5)$$

where σ_{ij} is the Cauchy total stress in the combined solid and fluid mixture, and b_i the body force acceleration.

For the pore fluid, the equation of motion is

$$-\frac{\partial(np)}{\partial x_i} + n\rho^f b_i + R_i - n\rho^f \dot{v}_i^f = 0 \quad (6)$$

where p is the pore pressure (taken as positive when compressive), and R_i the viscous drag force of the soil skeleton acting on the fluid phase, which, according to Darcy's law, can be written

$$R_i = -n \frac{\gamma^f}{k} \dot{w}_i \quad (7)$$

where k is the Darcy permeability coefficient in isotropic condition, and γ^f the unit fluid weight.

Substituting Eqs.(4) and (7) in Eq.(6) gives

$$\frac{\partial(np)}{\partial x_i} - n\rho^f b_i + n\gamma^f k_{ij}^{-1} \dot{w}_i + \rho^f \left(n\ddot{u}_i + \left(\frac{\partial \dot{w}_i}{\partial t} + \dot{w}_k \frac{\partial \dot{w}_i}{\partial x_k} \right) \right) = 0 \quad (8)$$

We assume that the acceleration of the fluid phase relative to the soil skeleton can be neglected. The u-p approximation (Zienkiewicz et al., 1982 and 1984) is valid for a low frequency dynamic analysis problem. The equations of motion for the total mixture given by Eq.(5) can be simplified to

$$\frac{\partial \sigma_{ji}}{\partial x_j} + \rho b_i - \rho \ddot{u}_i = 0 \quad (9)$$

and the pore fluid motion equation (8) rewritten as

$$\frac{\partial(np)}{\partial x_i} - n\rho^f b_i + n\gamma^f k^{-1} \dot{w}_i + n\rho^f \ddot{u}_i = 0 \quad (10)$$

Defining the excess pore pressure p_E , by

$$\frac{\partial(np - np_E)}{\partial x_i} = n\rho^f b_i \quad (11)$$

Eq.(10) becomes

$$\frac{\partial(np_E)}{\partial x_i} + n\gamma^f k^{-1} \dot{w}_i + n\rho^f \ddot{u}_i = 0 \quad (12)$$

From Eq.(12), we obtain

$$\dot{w}_i = -\frac{k}{\gamma^f} \left(\frac{1}{n} \frac{\partial(np_E)}{\partial x_i} + \rho^f \ddot{u}_i \right) \quad (13)$$

2.3 Continuity equation

According to the law of mass conservation, the continuity

equation of the soil skeleton in the local form is

$$\frac{\partial(\rho^s(1-n))}{\partial t} + \frac{\partial(\rho^s(1-n)v_i^s)}{\partial x_i} = 0 \quad (14)$$

Similarly, for the fluid it is

$$\frac{\partial(n\rho^f)}{\partial t} + \frac{\partial(n\rho^f v_i^f)}{\partial x_i} = 0 \quad (15)$$

After manipulation (Oka, et al., 1994), Eqs.(14) and (15) give

$$\frac{\partial \dot{w}_i}{\partial x_i} + l_{ii} + n \frac{\dot{\rho}^f}{\rho^f} + (1-n) \frac{\dot{\rho}^s}{\rho^s} = 0 \quad (16)$$

where l_{ij} is the symmetric rate of the deformation tensor. ρ^s is constant and $\dot{\rho}^s$ is zero because soil skeletons are assumed to be incompressible. $\dot{\rho}^f$ is the material derivative of the fluid phase density related to the material derivative, \dot{p}_E , of the excess pore pressure;

$$\dot{\rho}^f = \frac{\dot{p}_E}{K^f} \rho^f \quad (17)$$

where K^f is the bulk modulus of the fluid phase.

Substituting Eq.(17) in Eq.(16) gives

$$\frac{\partial \dot{w}_i}{\partial x_i} + l_{ii} + \frac{n}{K^f} \dot{p}_E = 0 \quad (18)$$

From Eq.(13) the sum of the partial derivatives of \dot{w}_i with respect to the coordinate x_i is

$$\begin{aligned} \frac{\partial \dot{w}_i}{\partial x_i} = & -\frac{k}{g} \left(l_{ii} + \frac{1}{\rho^f} \left(\frac{\partial^2 p_E}{\partial^2 x_i} \right)_i \right) - \frac{k}{g} \left(\frac{1}{n\rho^f} \frac{\partial p_E}{\partial x_i} - \frac{1}{(\rho^f)^2} \frac{\partial p_E}{\partial x_i} \frac{\partial \rho^f}{\partial x_i} \right. \\ & \left. + \frac{p_E}{n\rho^f} \left(\frac{\partial^2 n}{\partial^2 x_i} \right) - \frac{p_E}{n(\rho^f)^2} \frac{\partial n}{\partial x_i} \frac{\partial \rho^f}{\partial x_i} - \frac{p_E}{n^2 \rho^f} \frac{\partial n}{\partial x_i} \frac{\partial n}{\partial x_i} \right) \end{aligned} \quad (19)$$

where g is the acceleration caused by gravity.

From Eq.(17),

$$\frac{\partial p_E}{\partial x_i} = K^f \frac{\partial(\ln \rho^f)}{\partial x_i} \quad (20)$$

The porosity distribution is assumed to be smooth enough in the soils, therefore satisfying

$$\left(\frac{\partial^2(\ln n)}{\partial x_i^2} \right)_i = 0 \quad (21)$$

If the gradients of $\ln(n)$ and $\ln(\rho^f)$ are so small that their quadratic terms in the above expressions can be ignored, considering Eq.(21), then Eq.(19) is expressed by

$$\frac{\partial \dot{w}_i}{\partial x_i} = -\frac{k}{g} \left(l_{ii} + \frac{1}{\rho^f} \left(\frac{\partial^2 p_E}{\partial^2 x_i} \right)_i \right) \quad (22)$$

Finally, substituting Eq.(22) in Eq.(18), the final form of the continuity equation is

$$\frac{k}{g} \dot{l}_{ii} - l_{ii} + \frac{k}{\gamma^f} \left(\frac{\partial^2 p_E}{\partial^2 x_i} \right)_i - \frac{n}{K^f} \dot{p}_E = 0 \quad (23)$$

Clearly, Eqs.(14) and (23), together with the constitutive law,

define a coupled set of equations for saturated soils, in which u_i and p_E are the only unknown variables.

2.4 u-p equations in spatial discrete form

The equilibrium equation is satisfied at the end of each time step, $t + \Delta t$. In the updated Lagrangian method, relevant quantities, such as stress and strain, are correlated with the reference configuration at time t , and the weak formulation of Eq.(9) is

$$\int_{t_V} \rho^f \dot{u}_i \delta v_i d^3V + \int_{t_V} \left(\int_t^{t+\Delta t} \dot{S}_{ij} dt \right) \delta \dot{E}_{ij} d^3V + \int_{t_V} {}^t \sigma_{ij} \delta \dot{E}_{ij} d^3V = {}^{t+\Delta t} \mathbf{F} \quad (24)$$

where ${}^t \sigma_{ij}$ is the Cauchy stress tensor at time t , \dot{S}_{ij} the second Piola-Kirchhoff stress rate, \dot{E}_{ij} the Lagrangian strain rate tensor, and ${}^{t+\Delta t} \mathbf{F}$ the external virtual work done by the applied body forces and tractions. Let ${}^{t+\Delta t} b_i$ be the force acceleration per unit volume and ${}^{t+\Delta t} t_i$ the traction, then ${}^{t+\Delta t} \mathbf{F}$ is

$${}^{t+\Delta t} \mathbf{F} = \int_{t+\Delta t A} {}^{t+\Delta t} t_i \delta v_i d^{t+\Delta t} A + \int_{t+\Delta t V} \rho^f {}^{t+\Delta t} b_i \delta v_i d^{t+\Delta t} V \quad (25)$$

Integrating Eq.(23) for element volume gives

$$\begin{aligned} \int_{t_V} \rho^f \dot{l}_{ii} d^3V - \int_{t_V} \frac{\gamma^f}{k} l_{ii} d^3V + \int_{t_V} \left(\frac{\partial^2(p_E)}{\partial x_i^2} \right)_i d^3V \\ - \int_{t_V} \frac{n\gamma^f}{kK^f} \dot{p}_E d^3V = 0 \end{aligned} \quad (26)$$

By means of the FE-FE coupled method (Oka et al, 1991 and 1994), the terms associated with excess pore pressure in Eq.(26) are discretized by the finite difference method in the space domain in a grid pattern that is the same as that of the mesh for the finite element method. By the Gauss theorem, the third term on the left side of Eq.(26) becomes

$$\int_{t_V} \nabla^2 p_E d^3V = \oint_{t_A} \frac{\partial p_E}{\partial x_i} n_i d^3A \quad (27)$$

where 'A' is the element surface and n_i the normal direction vector of 'A'.

The value of the partial derivative $\partial p_E / \partial x_i$ on the common boundary of two elements is approximated by a difference expression in terms of excess pore pressure values at the gravity centers of the element and adjacent elements. It is calculated by

$$\oint_{t_A} \frac{\partial p_E}{\partial x_i} n_i d^3A \approx p_E \sum_{i=1}^6 (\mathbf{n}_i^A \cdot \mathbf{n}_i^E) A_i + \sum_{i=1}^6 p_{Ei} (\mathbf{n}_i^A \cdot \mathbf{n}_i^{Ei}) A_i \quad (28)$$

where p_E is the excess pore pressure value at the gravity center of the element; p_{Ei} that of the adjacent element; A_i the area of the

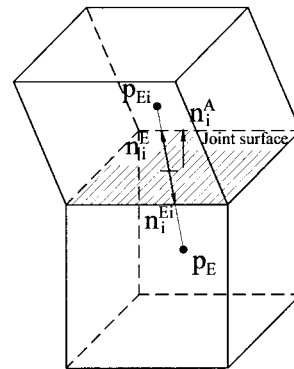


Fig. 1 Dissipation pore water between elements

joint surface between the element and the adjacent one i ; \mathbf{n}_i^Δ the normal direction vector of A ; \mathbf{n}_i^E the normal direction vector of dissipation from the element to the adjacent one i ; \mathbf{n}_i^{Ei} the normal direction vector of dissipation from the adjacent element i to the element (Fig.1).

3. A POSTERIORI ERROR ESTIMATE

Error estimate is the first and most important procedure in adaptive FE analysis. It indicates the next step, the mesh refinement. A posteriori error estimate procedure based on evaluating the L_2 -norm of variable error and the superconvergent patch recovery (SPR) procedure (Zienkiewicz and Zhu, 1992) was used in this study. The formulations were derived for linear hexahedral elements. A simple example of compression of saturated soil was analyzed in order to discuss the convergence of this error estimator.

3.1 Definition and evaluation of error

Error is defined as the difference between the exact solution and the finite element approximation value. Variables considered in the error estimate are displacement, strain, and stress. For example, an error in strain (Kelly, et al., 1983) is described as

$$e_\varepsilon = \varepsilon^* - \varepsilon^h \quad (29)$$

where ε^* represents exact solutions and ε^h the values of finite element approximation.

A one-dimensional linear approximation of strain ε^h and ε^* is shown in Fig.2 to explain the approximate value of FEM and exact solution.

The direct definitions of error given by Eq. (29) are not convenient for use in the process of error estimation. Usually, scalar norms, such as energy or L_2 norms, are used to measure error. Scalar measure corresponds to the square root of the quadratic error. In this study, the L_2 norm was used to measure error, as it is associated with errors of any quantity. For the strain in element i , the L_2 norm of the error, $\|e_\varepsilon\|_i$, is defined as

$$\|e_\varepsilon\|_i = \left(\int_{V_i} \{e_\varepsilon\}_i^T \{e_\varepsilon\}_i dv / V_i \right)^{1/2} \quad (30)$$

The error of entire solution domain $\|e_\varepsilon\|$ is calculated by summing the errors of all the elements.

$$\|e_\varepsilon\| = \left(\sum_{i=1}^{nel} \|e_\varepsilon\|_i^2 \right)^{1/2} \quad (31)$$

where nel is the total number of elements.

Generally, a relative error is used in the practical adaptivity process because it is more easily interpreted. The relative error of the solution is estimated by use of the error norm and strain L_2 -

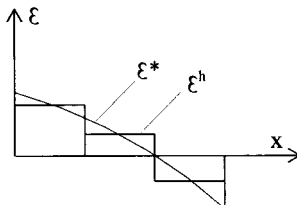


Fig. 2 Approximate values and exact solution

norm for the entire solution domain. Its definition is

$$\eta = \frac{\|e_\varepsilon\|}{\sqrt{\|e_\varepsilon\|^2 + \|\varepsilon^h\|^2}} \quad (32)$$

where

$$\|\varepsilon^h\| = \left(\sum_{i=1}^{nel} \|\varepsilon^h\|_i^2 \right)^{1/2} \quad (33)$$

The local error indicator for the i -th element is defined similarly. Clearly, the energy and L_2 norms are related to the strain energy,

$$\eta_i = \frac{\|e_\varepsilon\|_i}{\sqrt{\|e_\varepsilon\|_i^2 + \|\varepsilon^h\|_i^2} / nel} \quad (34)$$

3.2 Smoothing algorithm with superconvergent patch recovery

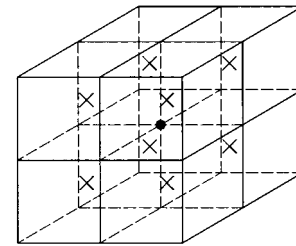
In the error estimate process, the relatively accurate values rather than the exact solution are used to calculate errors because the exact solution is not easy or impossible to obtain. The superconvergent patch recovery technique (Zienkiewicz and Zhu, 1992) was used. It is a single, continuous polynomial expansion of the function describing the derivatives and used in an element patch surrounding nodes at which recovery is desired. This expansion can be made to fit the superconvergent points locally in a least squares manner or can simply be an L_2 projection of the consistent finite element derivatives. In this technique, nodal values are assumed to belong to a polynomial expansion of the same order as that presented in the shape function. This polynomial expansion is valid over an element patch surrounding the particular assembly node considered. Such a ‘‘patch’’ represents a union of elements containing the vertex node. A typical patch for three-dimensional hexahedral elements is shown in Fig.3. This polynomial expansion is used to obtain the nodal values of strain;

$$\bar{\varepsilon}^* = \{P\} \{a\}^T \quad (35)$$

where $\{P\}$ contains the appropriate polynomial terms, and $\{a\}$ is a set of unknown parameters. For the eight nodes the hexahedral element in three-dimensions

$$\{P\} = \{1, x, y, z, xy, yz, zx, xyz\} \quad (36)$$

$$\{a\} = \{a_1, a_2, a_3, \dots, a_8\} \quad (37)$$



× Gauss points
● Patch assembly point
Nodal value determined by SPR

Fig. 3 Three-dimensional superconvergent patch recovery for hexahedra elements

The unknown parameter vector $\{a\}$ of the expansion in Eq. (35) is determined by ensuring a least squares fit of this expansion to the existing set of superconvergent, or at least high accuracy, sampling points in the patch considered if such points are available.

$$F(a) = \sum_{i=1}^n (\epsilon^h(x_i, y_i) - \bar{\epsilon}^*(x_i, y_i))^2 = \sum_{i=1}^n (\epsilon_h(x_i, y_i) - \{P\}\{a\}^T)^2 \quad (38)$$

where (x_i, y_i) are co-ordinates of a group of sampling points and n is the total number of sampling points. The minimization condition of $F(a)$ implies that $\{a\}$ satisfies

$$\sum_{i=1}^n \{P^T(x_i, y_i)P(x_i, y_i)\}\{a\}^T = \sum_{i=1}^n \epsilon^h(x_i, y_i)\{P^T(x_i, y_i)\} \quad (39)$$

This can be solved in matrix form as

$$\mathbf{a} = \mathbf{A}^{-1}\mathbf{b} \quad (40)$$

where

$$\mathbf{A} = \sum_{i=1}^n \mathbf{P}^T(x_i, y_i)\mathbf{P}(x_i, y_i) \quad \text{and} \quad \mathbf{b} = \sum_{i=1}^n \mathbf{P}^T(x_i, y_i)\epsilon^h(x_i, y_i);$$

$$\mathbf{P}(x_i, y_i) = \{P(x_i, y_i)\}$$

The discrete expression form for three-dimension hexahedra elements is:

$$\begin{bmatrix} \sum_i P_1(\xi'_i, \eta'_i, \zeta'_i)P_1(\xi'_i, \eta'_i, \zeta'_i) & \cdots & \sum_i P_1(\xi'_i, \eta'_i, \zeta'_i)P_8(\xi'_i, \eta'_i, \zeta'_i) \\ \vdots & \ddots & \vdots \\ \sum_i P_8(\xi'_i, \eta'_i, \zeta'_i)P_1(\xi'_i, \eta'_i, \zeta'_i) & \cdots & \sum_i P_8(\xi'_i, \eta'_i, \zeta'_i)P_8(\xi'_i, \eta'_i, \zeta'_i) \end{bmatrix} \begin{Bmatrix} a_1 \\ \vdots \\ a_8 \end{Bmatrix} = \begin{Bmatrix} \sum_i P_1(\xi'_i, \eta'_i, \zeta'_i)\epsilon_i^h \\ \vdots \\ \sum_i P_8(\xi'_i, \eta'_i, \zeta'_i)\epsilon_i^h \end{Bmatrix} \quad (41)$$

where $(\xi'_i, \eta'_i, \zeta'_i)$ are the normalized coordinates of a group of sampling points in three-dimensions.

3.3 Convergence of error estimator in three-dimension

A simple example was calculated to test this error estimator in three-dimensions. A $3 \times 3 \times 3\text{m}^3$ cubic block of saturated soil in a container had a vertical load applied to the top surface locally (Fig.4). The load was increased linearly to 90kN/m^2 until $t=0.3\text{second}$. Only the upper surface was drained. Two load cases are shown in Fig.4. In case 1, the load was applied to an area with $1 \times 1\text{ m}^2$ in corner. In case 2, the load is applied to an area with

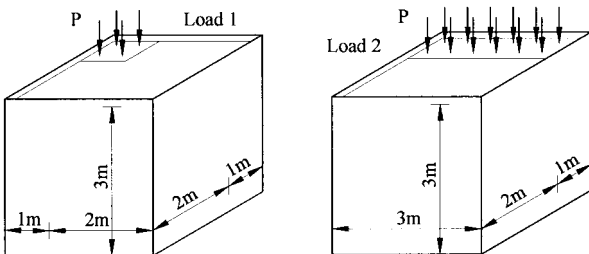


Fig. 4 Local compression of soil with Loads 1 and 2

$1 \times 3\text{ m}^2$ beside a side. Three meshes with 27, 216, and 729 elements were analyzed. For the boundary constraints of these meshes, the bottom nodes were fixed, and the nodes on side surfaces allowed to slide on the surfaces.

Figs.5-7 show the 27-, 216- and 729-element meshes and the respective error contour results for Load 1. Figs.8-10 show the 27-, 216- and 729-element meshes and their respective error contour results for Load 2. The relative error of an element was calculated at its center and the contour obtained by interpolation from the relative error values at the nodes. By comparing the average relative error values of the meshes with different quality levels, the relative error of the coarse mesh is readily shown to be larger than that of the fine mesh. In addition to the point with the peak value of relative error, the estimation of relative error is affected by the size of the element. When the size is small, the distance between the center of the element and point with the peak value is short, and the relative error of this element approaches the peak value. In contrast, the relative error of this element in the coarse mesh does not accurately approach the peak value. This is why the relative error value of a fine mesh is larger than that of a coarse mesh at some points. This phenomenon occurs in comparisons between meshes with small differences in mesh quality levels but evidently does not affect the average relative value of the entire mesh.

In Fig.11, the lines show the relationship between nodes number and the average relative error value, η_{m} , calculated by Eq.

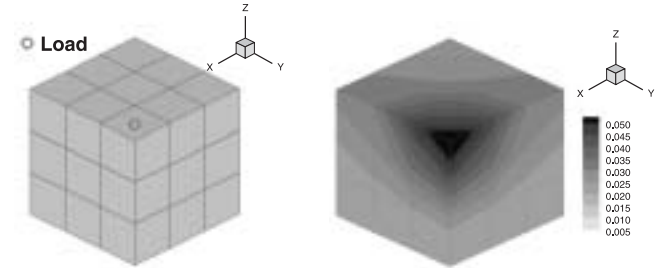


Fig. 5 Mesh, load, and error contour in Load 1 (27 elements)

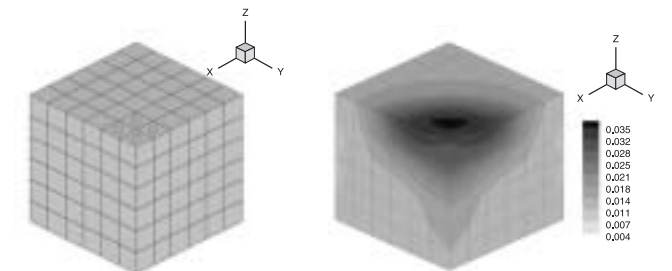


Fig. 6 Mesh, load, and error contour in Load 1 (216 elements)

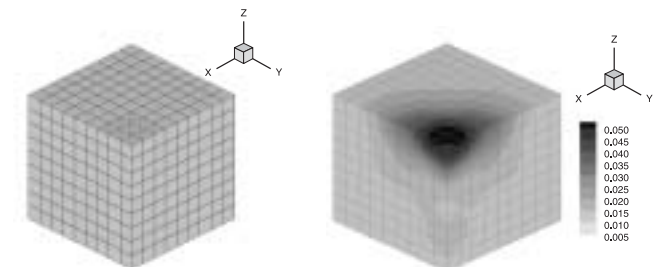


Fig. 7 Mesh, load, and error contour in Load 1 (729 elements)

(32) for two load cases. The rate of convergence in the L_2 -norm of strain is of the order $O(h^p)$. p is the degree of the polynomial utilized in the finite element approximation, for linear element $p=1$; h the size of the element; and h^{ndim} is proportional to the volume, where $ndim$ is the number of spatial dimensions in the problem (in three dimensions, $ndim=3$). The number of nodes or elements is inversely proportional to the volume. The rate of convergence therefore is $O(h^{1/3})$. The rates of convergent obtained by this error estimator are almost same as the theoretical values.

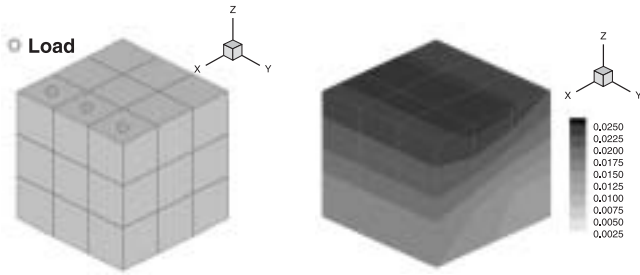


Fig. 8 Mesh, load, and error contour in Load 2 (27 elements)

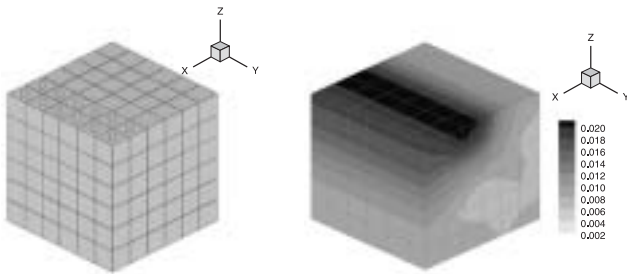


Fig. 9 Mesh, load, and error contour in Load 2 (216 elements)

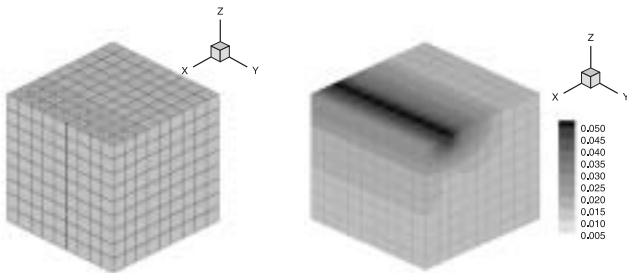


Fig. 10 Mesh, load, and error contour in Load 2 (729 elements)

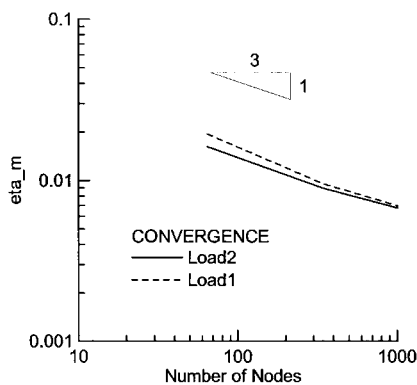


Fig. 11 Convergence of error estimator in three-dimensions

4. ADAPTIVE MESH REFINEMENT

A fission procedure belonging to h -refinement was applied to adaptive mesh refinement. Details of this procedure, including implementation for quadrilateral elements in two-dimensions and for hexahedral elements in three-dimensions, are presented here. Its application to soil-pile interaction analysis also is shown. A simple example was calculated to test the use of adaptive mesh refinement with the fission procedure.

4.1 3-D fission procedure for linear hexahedra elements

Linear hexahedral elements were used in the three-dimensional adaptive finite element analysis. When element error exceeded an acceptable limit, the element was fissioned into eight smaller elements, as shown in Fig.12. The circled numbers show element numbers, the other numbers node numbers. The initial mesh shown is mesh-a. After error estimation, the relative error for element 3 exceeded the error limit, and the element was fissioned into eight smaller elements: 3, 8-11. Nineteen new nodes, 19-37, were created: in the middle of each of the twelve sides, at the centers of the six surfaces and center of each element. The new refined mesh shown is mesh-b. The parameters of element 3 in mesh-a were transferred to elements 3, 5-11 in mesh-b, and the variables of the new elements interpolated from the variables of element 3 in mesh-a. Pore pressure values of the new smaller elements are the same as the value of the old parent element. The displacement, velocities, and accelerations of the new nodes also were interpolated from values of the old nodes in mesh-a. The next calculation step is based on mesh-b.

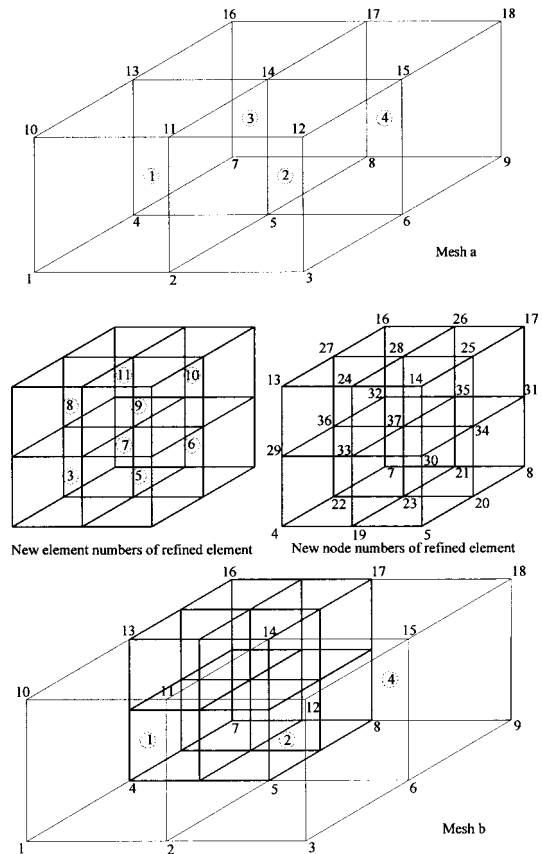


Fig. 12 Fission procedure of hexahedral elements

When an element is fissioned next to an unfissioned one, slave nodes are created that are constrained by the compatibility condition of the master node. There are two kinds of slave nodes. One is a slave node on the side of an element (Fig.13). Motion of slave node 0 should be governed by master node 1 and node 2 as

$$\mathbf{V}_3 = \mathbf{T}\{\mathbf{V}_1 \ \mathbf{V}_2\}^T \tag{42}$$

where \mathbf{T} is defined by $[\mathbf{I}/2, \mathbf{I}/2]$, in which \mathbf{I} is a unit matrix.

The equation of motion is not evaluated at the slave node. Instead, nodal forces at the slave nodes are added to the forces at the corresponding master nodes;

$$\{\mathbf{F}_1 \ \mathbf{F}_2\} = \{\mathbf{F}_1 \ \mathbf{F}_2\}^* + \mathbf{T}\mathbf{F}_3 \tag{43}$$

where \mathbf{F}_3 denotes nodal forces at the slave node and $\{\mathbf{F}\}^*$ those at nodes 1 and 2 prior to the consideration of \mathbf{F}_3 .

The second type is a slave node on the surface of the element (Fig.14). Motion of slave node 0 should be governed by the master node 1 up to node 4;

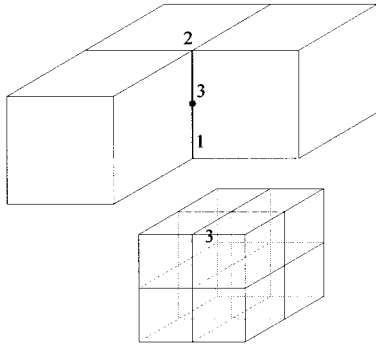


Fig. 13 Slave node on the side of an element

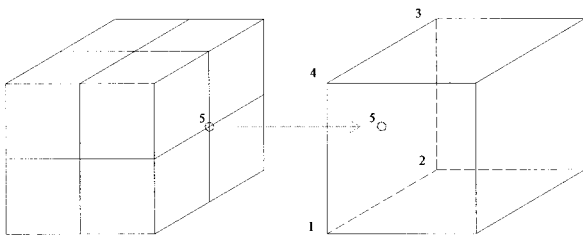


Fig. 14 Slave node on the surface of an element

$$\mathbf{V}_5 = \mathbf{T}\{\mathbf{V}_1 \ \mathbf{V}_2 \ \mathbf{V}_3 \ \mathbf{V}_4\}^T \tag{44}$$

where \mathbf{T} is defined by $[\mathbf{I}/4, \mathbf{I}/4, \mathbf{I}/4, \mathbf{I}/4]$, in which \mathbf{I} is a unit matrix. The equation of motion is not evaluated at the slave node. Instead, nodal forces at slave nodes are added to the forces at the corresponding master nodes;

$$\{\mathbf{F}_1 \ \mathbf{F}_2 \ \mathbf{F}_3 \ \mathbf{F}_4\} = \{\mathbf{F}_1 \ \mathbf{F}_2 \ \mathbf{F}_3 \ \mathbf{F}_4\}^* + \mathbf{T}\mathbf{F}_5 \tag{45}$$

where \mathbf{F}_5 denotes nodal forces at the slave node and $\{\mathbf{F}\}^*$ those at nodes 1 and 2 prior to the consideration of \mathbf{F}_5 .

An array NABOR (NE, I, J) is used to define the relationship of neighbor elements. It is composed of the twenty-four neighboring elements on the six joint surfaces with other elements. NE is element number. I surface number and J neighbor element number defined in Fig.15.

To clarify use of the array, consider mesh-a and mesh-b (Fig.12) and the fission of element 3. NABOR arrays for elements 1 and 3 are given in Table 1 for both meshes. Zero indicates the boundary at the surface of an element. The four identical numbers on a surface indicate only one neighbor element on that surface. When an element is beside fissioned elements, all the numbers of the four neighboring elements on this surface are recorded in the array.

4.2 Modifying permeance of pore water between hexahedral elements

If an unfissioned element is beside a fissioned element, the usual permeance route crossing the intersurface should be modified, as shown in Fig.16. The place of permeance between two unfissioned elements is taken by the permeance between an unfissioned element and four fissioned elements. The terms describing the permeance of pore water in the continuity equation therefore are modified easily.

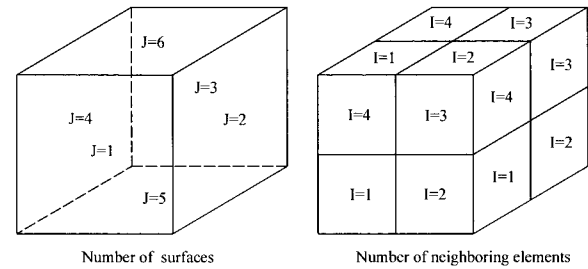


Fig. 15 Definition of I and J for array NABOR (NE,I,J)

Table 1 Nabor (JE,I,J) for mesh-a and mesh-b

mesh	JE	J=1,I=1:4	J=2,I=1:4	J=3,I=1:4	J=4,I=1:4	J=5,I=1:4	J=6,I=1:4
a	1	0,0,0,0	2,2,2,2	3,3,3,3	0,0,0,0	0,0,0,0	0,0,0,0
b	1	0,0,0,0	2,2,2,2	3,5,8,9	0,0,0,0	0,0,0,0	0,0,0,0
a	3	1,1,1,1	4,4,4,4	0,0,0,0	0,0,0,0	0,0,0,0	0,0,0,0
b	3	1,1,1,1	5,5,5,5	7,7,7,7	0,0,0,0	0,0,0,0	8,8,8,8

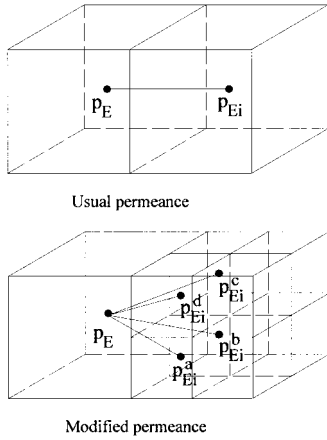


Fig. 16 Modifying permeance of pore water in three dimensions

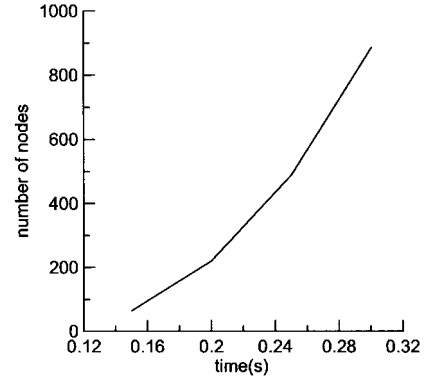


Fig. 18 Increase in node number

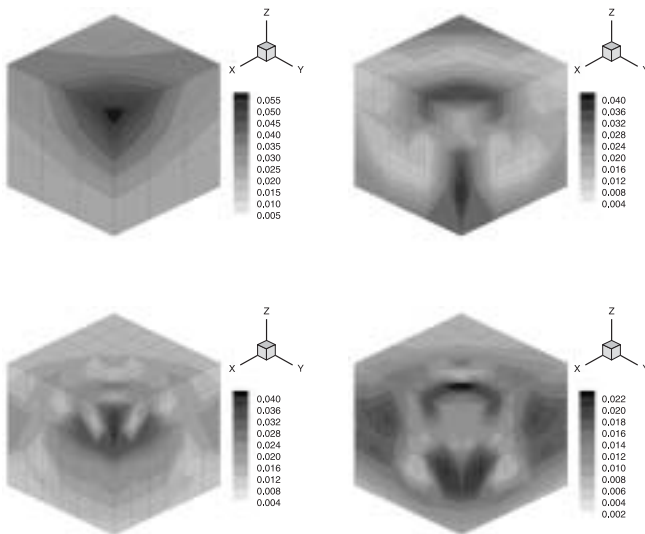


Fig. 17 Refined meshes and relative error contours at different steps

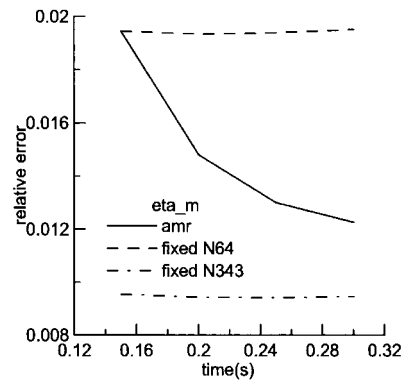


Fig. 19 Decrease in relative error

4.3 3-D Soil block compression

A simple three-dimensional example was analyzed to test the adaptive mesh refinement method. The example model is same as that used to check the error estimator in section 3.3. The loading condition is Load 1. *h*-Adaptive FE analysis starts from an initial mesh with 27 elements, and the relative error limit is defined as 0.02. Mesh refinement starts at $t=0.15$ second. The time increment of finite element calculation is 0.01 second. Mesh refinement is implemented every five steps in the finite element calculation. The initial and refined meshes at three steps of adaptive mesh refinement with relative error contours are shown in Fig.17. Elements whose relative errors are larger than the 0.02 limit are refined in every step of adaptive refinement.

Fig.18 shows that the number of elements increases rapidly. At the same time, relative error decreases, as shown in Fig.19 in which amr denotes results of the adaptive FE method. Because deformation is very small, relative error does not appear to increase evidently. Fig.20 shows the efficacy of the method. The results obtained show that this adaptive scheme produces substantial improvements in accuracy with limited computation.

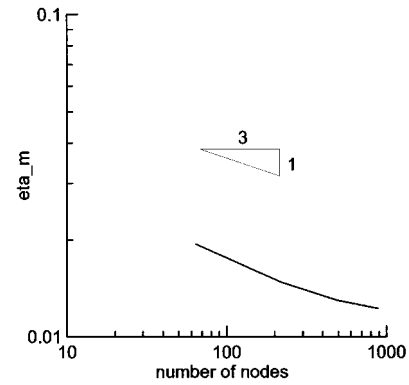


Fig. 20 Convergence of error

5. NUMERICAL EXAMPLE

Three-dimensional seismic analysis of an embankment by the *h*-adaptive FE method is introduced. The updated Lagrangian formulation was adopted for the governing equations of the finite element method to deal with large deformation of liquefied soil. An effective cyclic elasto-plastic model was used to describe the material nonlinearity of saturated soil.

An embankment constructed on saturated sand is shaken by an earthquake in the *x*-direction. As shown in Fig. 21, the embankment is 8m wide at the top and 16m wide at the bottom. There is a type of filling soil without pore water in this embankment composed of Edosaki sand 1. The foundation soil region assessed is

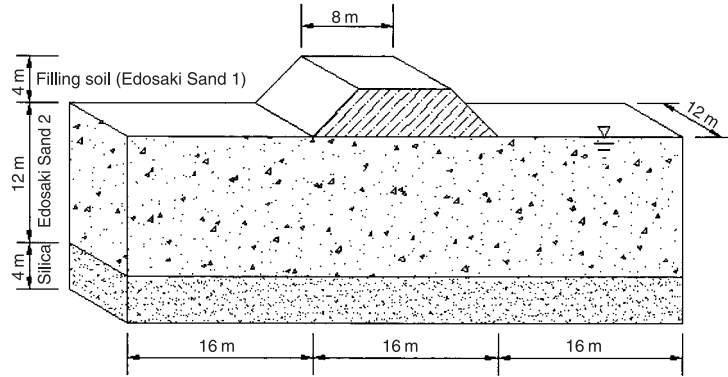


Fig. 21 Embankment example of 3-D analysis considering large deformation

Table 2 Soil parameters of the embankment example

Material parameter	Edosaki sand 1	Edosaki sand 2	Filling soil silica
Density $\rho(t/m^3)$	1.75	1.857	1.990
Coefficient of permeability $k(m/s)$	-	1.7E-5	2.5E-5
Initial void ratio e_0	0.856	0.856	0.676
Compression index λ	0.0264	0.0264	0.0250
Swelling index κ	0.0055	0.0055	0.0025
Initial shear modulus ratio G_0/σ_{m0}	829	829	1280
Over consolidation ratio OCR	1.0	1.0	1.0
Phase transformation stress ratio M_m	0.91	0.91	0.91
Failure stress ratio M_f	1.12	1.12	1.51
Hardening parameter B_0	3000	3000	5000
Hardening parameter B_1	0.0	0.0	0.0
Hardening parameter C_f	-	60	100
Plastic reference strain γ^p	-	0.01	0.004
Elastic reference strain γ^E	-	0.03	0.09
Dilatancy parameter D_0	0.0	5	1.2
Dilatancy parameter n	0.0	1.2	4.0

48m wide, 12m thick, and 16m deep. If an area larger than this is considered, deformation caused by liquefaction obviously will be larger but only by a small extent. There are two kinds of saturated soil, Edosaki sand 2 and silica, in the soil layers. The upper layer is composed of Edosaki sand 2 that is 12m deep. The bottom layer of silica is 4m deep. Dynamic parameters of these soils are given in Table 2. Soil parameters were obtained experimentally and by evaluation. The parameter definitions are those introduced by Oka et al. (1992). Initial stresses of the elements were calculated for

gravity. A linear hexahedral element with eight nodes was used. Displacement of the bottom boundary was fixed, the side boundary was fixed horizontally but allowed to slide on the surface. Drainage was allowed only on the top boundary surface of the mesh.

Input earthquake acceleration was a modified earthquake acceleration history at 60% amplitude of the original record, Fig. 22. The original acceleration was recorded in the 1995 Hyogoken-Nanbu earthquake. The maximum value is 433 gal. Fig. 23 gives the time history of the EPWPR of soil 6m deep. Reduction of the

effective soil stress due to the increased excess pore water pressure ratio leads to significant loss of soil strength and stiffness. When the excess pore water pressure ratio reaches 1.0, full liquefaction occurs at about 6 second.

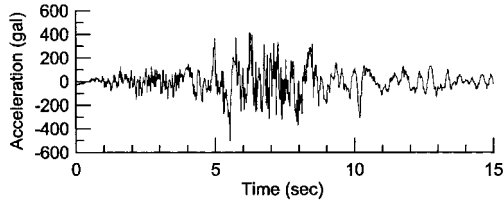


Fig. 22 Input acceleration for a 3-D embankment

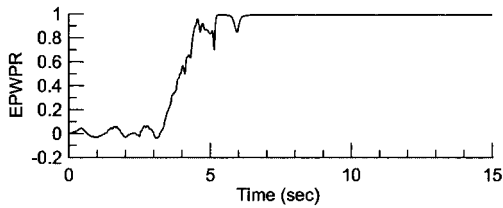


Fig. 23 EPWPR response of the 3-D embankment example

The deformed meshes and their respective relative error distributions at $t=7.0, 11.0,$ and 15.0 seconds analyzed with a fixed coarse mesh (168 elements) are given in Fig.24. (a), (b) and (c). The L_2 -norm of strain was used to evaluate the error. Deformation and strain in regions besides the foot of and under the embankment are larger than in other area, and relative error values in those area are increased.

The adaptive mesh refinement process starts at $t=6.5$ seconds for the initial coarse mesh with 168 elements. The relative error limit is 0.07. Adaptive mesh refinement was done once per second, and the time increment of finite element calculation was 0.005 second. Only two levels of refinement were allowed, which means that an element is fissioned only twice. The refined meshes analyzed by the h -adaptive FEM using the updated Lagrangian method at times $t=7.0, 11.0,$ and 15.0 seconds respectively are shown in Fig.25. (a), (b) and (c).

Elements in regions with large errors were refined step by step. The relative error value of the refined mesh decreased as the elements were fissioned. In three-dimensional adaptive analysis, as the mesh becomes fine, the number of elements increases rapidly. No relative error value larger than the 0.07 limit is found in the mesh with an adaptive level lower than 2 in Fig. 25. (a), (b) and (c).

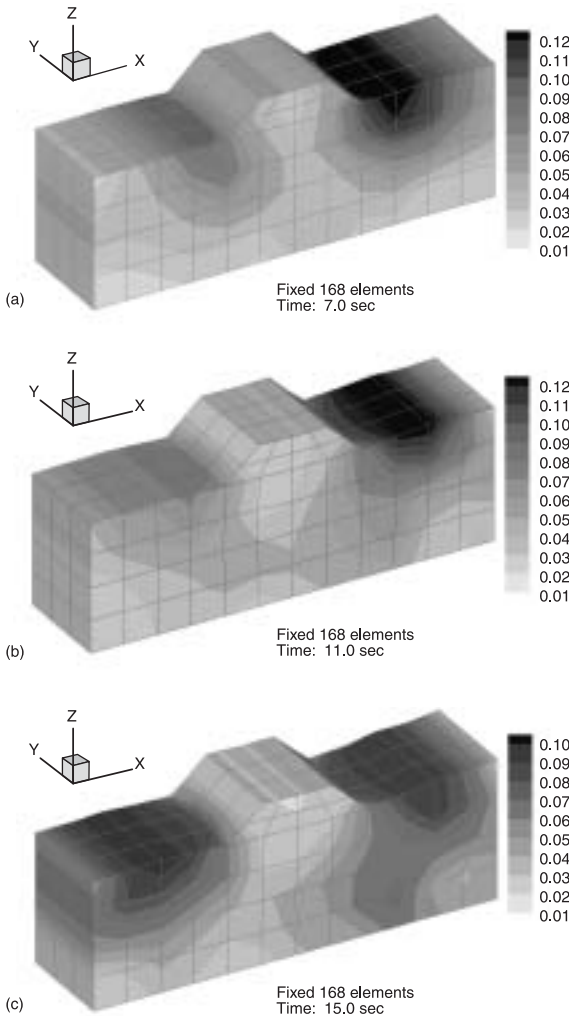


Fig. 24 Coarse mesh and relative error results for the 3-D embankment

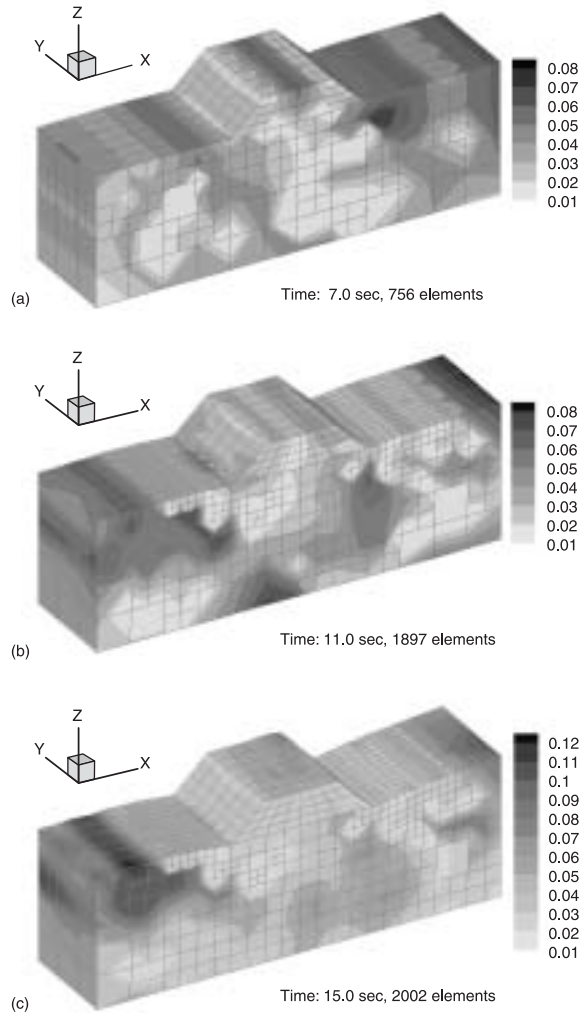


Fig. 25 Final mesh with adaptive mesh refinement

This example also was analyzed with a fixed fine mesh of 1344 elements and cubic, liquefiable soil elements with 2m-long sides. Meshes with relative error distributions at $t=7.0, 11.0$ and 15.0 seconds are shown respectively in Fig. 26. (a), (b) and (c). The relative error value of the fine mesh is lower than that of the fixed coarse mesh, and the top surface of the liquefiable soil much smoother. The high relative error value distribution also is concentrated in regions near the foot of or under the embankment where the elements have undergone large deformation and strain. The meshes of the adaptive FE analysis are similar to the meshes calculated with the fixed fine mesh. Clearly, the refinement of these elements improves the accuracy of embankment displacement results.

In Figs. 27 and 28, horizontal and vertical displacements on the top of the embankment use for the adaptive FE analysis are compared with those for finite element analysis with fixed coarse and fixed fine meshes without the adaptive procedure considering large deformation. Horizontal displacement on the top of the embankment, calculated with the fixed fine mesh, is larger than with the coarse mesh (Fig. 27). In contrast, vertical displacement on the top of the embankment calculated with the fixed fine mesh is smaller than with the coarse mesh (Fig. 28).

As mesh refinement proceeds, horizontal displacement calculated by the adaptive FE method becomes large, and vertical dis-

placement small and closer to the displacement values of the fixed fine mesh. As mesh refinement was not carried out before $t=6.5$ seconds, it is reasonable that the adaptive results are not as accurate as fine mesh results. From a comparison of the horizontal and vertical displacement lines for the three cases, it concluded that the h -adaptive FE method, which considers large deformation, effectively improves accuracy.

In Fig. 29, accuracies of three different cases are compared by showing the three the average relative errors curves. As the quality of the entire mesh affects seismic analysis results, the general quality of the entire mesh is determined by evaluating the average relative error. The average relative error of the fixed coarse mesh with 168 elements is larger than that of the fixed fine mesh with 1344 elements. In the adaptive FE analysis, the average relative error value decreased once the adaptive procedure started at $t=6.5$ seconds. As the adaptive process proceeds, the average relative error value approaches the value for the fixed fine mesh. Reduction of the average relative error confirms the efficacy of the

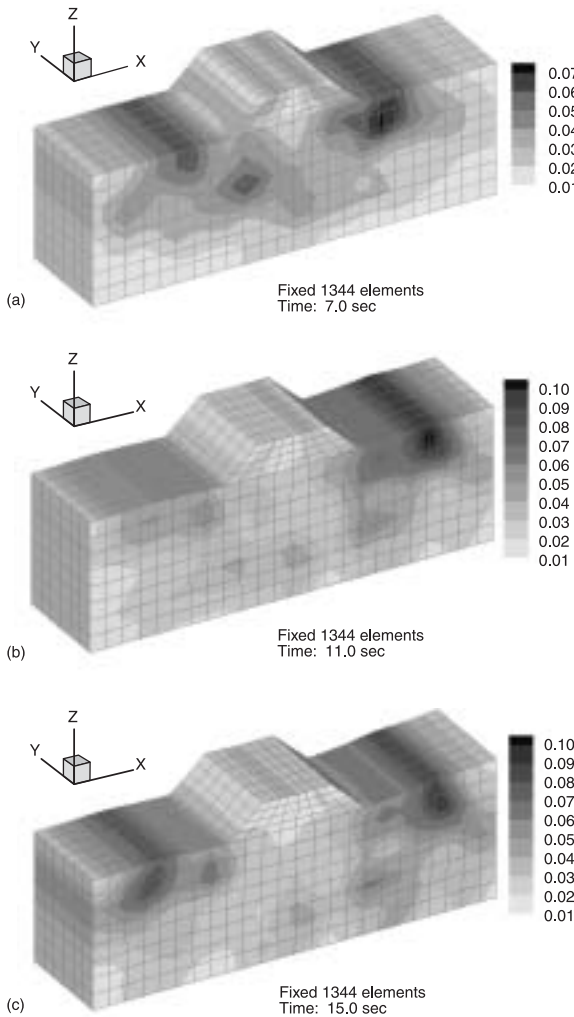


Fig. 26 Fixed fine mesh and relative error results

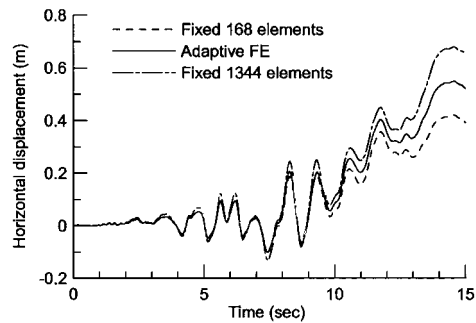


Fig. 27 Horizontal displacement on the top of the embankment for 3-D analysis

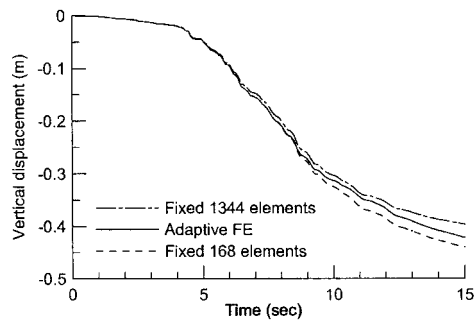


Fig. 28 Vertical displacement on the top of the embankment for 3-D analysis

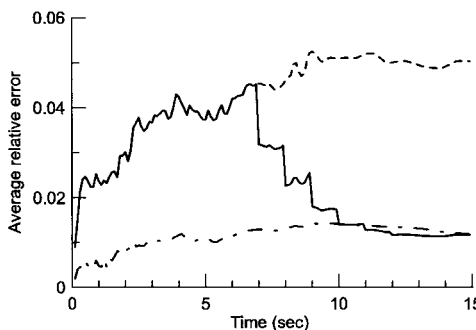


Fig. 29 Average relative error of 3-D analysis of the embankment

adaptive FE method.

By this example, the h -adaptive FE method was shown to be effective for three-dimensional elasto-plastic analysis of an embankment constructed on liquefiable soil. Moreover it improves the accuracy of the finite element analysis by reducing the size of large error elements.

6. CONCLUSION

The h -adaptive technique was applied to non-linear FE analysis of saturated soil considering large deformation that includes the liquefaction phenomenon. In previous research, adaptive techniques have been used to solve static or transient problems with monotonous loads. In this study, the adaptive FE method was applied to seismic analysis in which the load was an earthquake acceleration history that included a few thousands steps of time increments and cyclic vibration. The fission procedure belonging to h -refinement, indicated by element error estimate in the three-dimensional adaptive FE method was used. The approximation was refined successively, satisfying the predetermined standard of accuracy, and the efficacy of this method in finite element analyses was confirmed. This method is easily used to solve practical and engineering problems. In the transient analysis, the relative errors limits used ranged from 0.01 to 0.05. Although there have been few studies on the use of adaptive mesh refinement in dynamics analysis, the reported relative errors limits in dynamics analysis have ranged from 0.02 to 0.07. Selection of an appropriate adaptive frequency also is recommended.

A posteriori error estimate based on the L_2 norm of strain error was used in the adaptive FE method. It effectively estimated elements error after each calculation step in the nonlinear FE analyses of soil. The superconvergent patch recovery technique was used for the error estimates. The convergence of this error estimate method was tested with three-dimensional examples and different quality meshes. The convergence ratios matched the theoretical values. This method is readily implemented for any code, and calculations based on it are very simple. Moreover, the advantage of saving computation time is evident, and the technique is a reliable indicator in mesh refinement.

The h -adaptive FE method is well suited to the elasto-plastic analysis of saturated soil, especially to problems that include liquefaction analysis. Refining elements with large deformation or large error due to liquefaction flow effectively improves the accuracy of nonlinear numerical analysis. The h -adaptive FE method also is useful for three-dimensional dynamic analysis. The application of adaptivity to the three-dimensional nonlinear analysis of saturated soil is valuable for the development of adaptive techniques. By giving the limit of the adaptive level and selecting a suitable adaptive frequency, the calculation time is reduced and accuracy is increased. All the results obtained in this study show that this adaptive scheme produces substantial improvements in accuracy under a limited computational effort.

REFERENCES

- Akai, K. and Tamura, T. (1978). Study of two-dimensional consolidation accompanied by an elastic plastic constitutive equation, Proceedings

- of JSCE, No. 269, 98-104.
- Belytschko, T. and Tabbara, M. (1993). H -adaptive finite element methods for dynamic Problem, with Emphasis on Localization, International Journal for Numerical Methods in Engineering, Vol. 36, 4245-4265.
- Belytschko, T., Wong, B. L. and Plaskacz, E. J. (1989). Fission-fussion adaptivity in finite elements for nonlinear dynamics of shells, Computers & Structures, Vol. 33, 1307-1323.
- Biot, M. A. (1962). Mechanics of deformation and acoustic propagation in porous media, Journal of Applied Physics, Vol. 33, 1482-1498.
- De, J. P., Gago, S. R. Kelly, D., W., Zienkiewicz, O., C. and Babuska, I. (1983). A posteriori error analysis and adaptive processes in the finite element method: Part II-Adaptive mesh refinement, International Journal for Numerical Methods in Engineering, Vol. 19, 1621-1656.
- Di, Y. and Sato, T. (2001). Large deformation dynamic analysis of porous medium using FEM-FDM coupled method, Advances in Computational Engineering & Sciences (Atluri, S.N., Nishioka, T. and Kikuchi, M., Eds.), Chapter 12 Multiphysics & Multibody Dynamic, Tech Science Press (CD-ROM).
- Hamada, M., Sato, H. and Kawakami, T. (1994). A consideration of the mechanism for liquefaction-related large ground displacement, A proceedings from the fifth U.S.-Japan workshop on earthquake resistant design of lifeline facilities and countermeasures against soil liquefaction, Technical Report NCEER-94-0026, 217-232.
- Hicks, M., A. (2000). Coupled computations for an elastic-perfectly plastic soil using adaptive mesh refinement, International Journal for Numerical. Analysis Methods of Geomechanics, Vol. 24, 453-476.
- Kelly, D.W., De, J. P., Gago, S., R. Zienkiewicz, O., C. and Babuska, I. (1983). A posteriori error analysis and adaptive processes in the finite element method: Part I: Error analysis, International Journal for Numerical Methods in Engineering, Vol. 19, 1593-1619.
- Oka, F., Yashima, A., Shibata, T., Kato, M. and Uzuoka, R. (1994). FEM-FDM coupled liquefaction analysis of a porous soil using an elasto-plastic model, Applied Scientific Research, Vol. 52, 209-245.
- Oka, F., Yashima, A., Kato, M. and Sekiguchi, K. (1992). A constitutive model for sand based on the non-linear kinematic hardening rule and its application, Proceedings of 10th World Conference on earthquake Engineering, Barcelona, 2529-2534.
- Tang, X. and Sato, T. (2004). A posteriori error estimate and h -adaptive FE analysis of Liquefaction with large deformation, Journal of Geotechnical Engineering, No. 788/III-69, 1-15.
- Tang, X. and Sato, T. (2004). H -adaptivity applied to liquefiable soil in nonlinear analysis of soil-pile interaction, Proceedings of the 11th International Conference on Soil Dynamics & Earthquake Engineering & The 3rd International Conference on Earthquake Geotechnical Engineering, 760-767.
- Zienkiewicz, O. C. and Zhu, J. Z. (1992). The superconvergent patch recovery and a posteriori error Estimates. Part I: The Recovery Technique, International Journal for Numerical Methods in Engineering, Vol. 33, 1331-1364.
- Zienkiewicz, O. C. and Zhu, J. Z. (1992). The superconvergent patch recovery and a posteriori error estimates. Part II: Error estimates and adaptivity, International Journal for Numerical Methods in Engineering, Vol. 33, 1365-1382.
- Zienkiewicz, O. C. and Zhu, J. Z. (1992). The superconvergent patch recovery (SPR) and adaptive finite element refinement, Computational Methods and Application of Mechanics Engineering, Vol. 101, 207-224.